JOURNAL OF COMPUTATIONAL PHYSICS 86, 355–375 (1990)

The Multidimensional Positive Definite Advection Transport Algorithm: Nonoscillatory Option

PIOTR K. SMOLARKIEWICZ AND WOJCIECH W. GRABOWSKI*

National Center for Atmospheric Research,† Boulder, Colorado 80307

Received November 11, 1988; revised March 8, 1989

This paper presents a nonoscillatory option (i.e., free of dispersive ripples) of the advection algorithm described previously in *J. Comput. Phys.* (**54** (1984), 325; **67** (1986), 396). The approach adopted merges the flux-corrected transport methodology with the iterative formalism of the algorithm. Further discussion of the algorithm's accuracy is included. Theoretical considerations are illustrated through numerical tests and examples of applications to atmospheric fluid dynamics problems.

1. INTRODUCTION

Smolarkiewicz [1, 2] and Smolarkiewicz and Clark [3] described a class of nonlinear, fully multidimensional, sign-preserving advective transport algorithms of varying accuracy and levels of complexity. The general concept of the algorithm is that of the dissipative advection schemes; however, compensation of the leading truncation error terms of the donor-cell scheme is nonlinear. It is achieved through the iterative application of the donor-cell scheme where the second and following iterations use pseudo velocity fields, obtained from renormalization of the truncation errors of the donor-cell scheme into the form of donor-cell fluxes. The resulting conservative algorithm is second-order accurate for an arbitrary velocity field while it possesses such useful properties of the donor-cell scheme as strict conservation of the sign of the transported field and a relatively small phase-error. The analytic method of the derivation of the algorithm [2] allows for a relatively simple generalization of the scheme on nonstandard forms of the continuity equation with eventual inclusion of the diffusive terms [3].

In both [2, 3] it was emphasized that although the algorithm is strictly sign preserving it may, in general, suffer from dispersive ripples, similar to all higher order linear advection schemes. The sign-preserving property is associated with the nonoscillatory behavior of the algorithm near "zeros" of the transported field (Section 4 in [3]). When the transported field contains a significant constant or

* On leave from the Institute of Geophysics, Polish Academy of Sciences, Warsaw, Poland.

† The National Center for Atmospheric Research is sponsored by the National Science Foundation.

0021-9991/90 $3.00

background component then the dispersive ripples appear in the solutions. The amplitude of the oscillations is considerably reduced compared to the linear schemes. In a number of applications, monotonicity preservation becomes a necessary property of the advection scheme. In responding to such practical needs, we present an option of the multidimensional positive definite advection transport algorithm (hereinafter, MPDATA) which strictly preserves the local monotone character of the transported field. The approach adopted merges the flux-corrected transport (FCT) methodology of Boris and Book [4–6] and Zalesak [7] with the iterative formalism of MPDATA. Due to the original design of MPDATA it leads to the simple modification of the original version of the algorithm. Because of MPDATA's specific phase-error properties [3], the nonoscillatory option appears to be an accurate and competitive tool for applications. A practical advantage of the approach is separability of the sign and the monotonicity preservation. Because the sign preservation is about half as expensive as the monotonicity preservation, incorporating the nonoscillatory modification as an extra option of MPDATA in the dynamic model has economic advantages, especially in atmospheric flows where a class of problems requiring strict preservation of monotonicity is relatively narrow compared to the class of problems that require strict preservation of sign.

The paper is organized as follows. Section 2 contains a summary of MPDATA. Section 3 contains a summary of the general, arbitrary-dimensional FCT procedure together with the consequently following nonoscillatory version of MPDATA. Section 4 presents elementary tests and discussion on the accuracy of the scheme. The examples of application of the nonoscillatory option of MPDATA to atmospheric fluid dynamics problems are presented in Section 5.

2. Summary of Basic MPDATA

The basic equation to be solved is the continuity equation describing transport of a nondiffusive scalar quantity in M-dimensional space

$$\frac{\partial \psi}{\partial t} + \sum_{I=1}^{M} \frac{\partial}{\partial x^I}(\psi u^I) = 0, \tag{1}$$

where $\psi \equiv \psi(t, x^1, ..., x^M)$ is the nondiffusive scalar quantity, assumed to be of constant sign; $u^I \equiv u^I(t, x^1, ..., x^M)$ is the Ith velocity component, $I = 1, ..., M$; and t, $\mathbf{x} \equiv (x^1, ..., x^M)$ are the time- and space-independent variables. For compactness of the numerical equations we shall use the same notation as in [2, 3].

$\psi_{\mathbf{i}}^n$ is a numerical approximation of the solution of Eq. (1), defined in points $(t^n, \mathbf{x}_{\mathbf{i}})$, where $t^n = n \cdot \Delta t$, $\mathbf{x}_{\mathbf{i}} = (i^1 \Delta X^1, i^2 \Delta X^2, ..., i^M \Delta X^M)$, $n = 0, ..., NT$; $i^I = 0, ..., NX^I$, and ΔX^I is the constant spatial increment in the Ith direction. The indices described by capital letters always indicate vector components whereas the indices described by lowercase letters indicate grid positions.

$\mathbf{e}_I \equiv (0, 0, ..., 0, 1, 0, ..., 0)$ is a unity vector in the Ith direction;

${}^{n}u^{I}_{\mathbf{i}+1\,2\mathbf{e}_I}$ is the Ith velocity component in the nth time step defined on a staggered grid (the Ith component is staggered $\frac{1}{2}\Delta X^I$ in the Ith direction).

The basic MPDATA may be compactly written as

$$\psi_{\mathbf{i}}^{(*)^k} = \psi_{\mathbf{i}}^{(*)^{k-1}} - \sum_{I=1}^{M} \left[F^I(\psi_{\mathbf{i}}^{(*)^{k-1}}, \psi_{\mathbf{i}+\mathbf{e}_I}^{(*)^{k-1}}, u^{(\sim)^k}_{I\,\mathbf{i}+1\,2\mathbf{e}_I}) - F^I(\psi_{\mathbf{i}-\mathbf{e}_I}^{(*)^{k-1}}, \psi_{\mathbf{i}}^{(*)^{k-1}}, u^{(\sim)^k}_{I\,\mathbf{i}-1\,2\mathbf{e}_I})\right]. \tag{2}$$

where F^I is the donor-cell advective flux in the Ith direction evaluated in the same staggered points as the Ith velocity component and defined as

$$F^I(\psi_{\mathbf{i}}, \psi_{\mathbf{i}+\mathbf{e}_I}, u) \equiv ([u]^+ \psi_{\mathbf{i}} + [u]^- \psi_{\mathbf{i}+\mathbf{e}_I}) \frac{\Delta t}{\Delta X^I}. \tag{3}$$

$[\cdot]^+ \equiv \max(0, \cdot)$ and $[\cdot]^- \equiv \min(0, \cdot)$ are the positive- and the negative-part operators, respectively. $k = 1, \ldots, IORD$ numbers the corrective iterations $\psi_{\mathbf{i}}^{(*)}$ such that

$$\psi_{\mathbf{i}}^{(*)^0} \equiv \psi_{\mathbf{i}}^{n}; \qquad \psi_{\mathbf{i}}^{(*)^{IORD}} \equiv \psi_{\mathbf{i}}^{n+1} \tag{4a), (4b}$$

and also, defined for each consecutive iteration, pseudo velocities such that

$$u^{(\sim)^{k+1}} = \tilde{u}(u^{(\sim)^k}, \psi^{(*)^k}); \qquad u^{(\sim)^1}_{I\,\mathbf{i}+1\,2\mathbf{e}_I} \equiv {}^{n+1\,2}u^{I}_{\mathbf{i}+1\,2\mathbf{e}_I}. \tag{5a), (5b}$$

The pseudo velocities appearing in the symbolic relationship in (5a) are derived analytically based on the truncation error analysis of the donor-cell scheme (Section 2 in [2]). Their explicit, finite-difference representations were discussed in detail in [2, 3]. When $IORD = 1$ the algorithm results in the common donor-cell scheme. For details on the derivation of the algorithm as well as a discussion of consistency, stability, and accuracy, interested readers are referred to [2] In [2] it has been shown for $M \leqslant 3$, that the stability of the first iteration (the donor cell scheme) implies stability of the consecutive iterations. An extension of the scheme to the anelastic transport equation, which requires taking spatially variable density into account in (1), (2), and explicit representations of (5a), has been discussed in detail in [3, Section 3.3].

The scheme was originally designed for the transport of the constant-sign scalar variables in the anelastic, fluid dynamic model with inclusion of the moist convection processes [3]. Extension of the scheme to fields of variable sign may be achieved in several different ways, however, adding an appropriate constant to the transported field appears to be an optimal choice. This option has been discussed in detail (Section 4 in [3]), since it exposes an important property of the scheme. In contrast to (1) and the linear finite difference approximations to it, MPDATA *is not* invariant with respect to the addition of a constant, but

$$\text{MPDATA}[\psi + \text{const}] = \text{MPDATA}[\psi] + \mathcal{O}(\Delta X^2, \Delta t^2), \tag{6}$$

where MPDATA in (6) has a symbolic meaning of approximation to (1). In [3] it was shown that adding a large constant to the transported field *increases* overall accuracy of the solution, but at the cost of losing the nonoscillatory character of the solution near the background value. A possible cure of this deficiency of MPDATA incorporates the ideas of FCT algorithms [4–7].

3. The Nonoscillatory Option of the Scheme

3.1. *General FCT Procedure*

The generic reason for the appearance of the oscillations in the numerically generated higher order accurate solutions to Eq. (1) is that the magnitude of certain fluxes is overestimated with respect to their analytic value. In contrast, the magnitude of the fluxes given by the first-order accurate schemes is underestimated, which results in monotone but heavily damped solutions [7]. The FCT procedure overcomes the problem of false oscillations by imposing appropriate limits on the transport fluxes from the higher order accurate algorithms. In the following we summarize the essential aspects of the general FCT scheme, in order to facilitate derivation of the nonoscillatory option of MPDATA.

Consider some higher order advection algorithm for integration of Eq. (1),

$$\psi_{\mathbf{i}}^{n+1} = \psi_{\mathbf{i}}^{n} - \sum_{l=1}^{M} \left(FH^{l}_{\mathbf{i}+1/2\mathbf{e}_l} - FH^{l}_{\mathbf{i}-1/2\mathbf{e}_l}\right). \tag{7}$$

Since in (7) the time level of the fluxes may be taken at any position, this equation represents the general form of an arbitrary finite-difference flux-form scheme. The high-order FH-flux may be arbitrarily cast into a sum of the flux from a certain low-order nonoscillatory scheme and the residual, i.e.,

$$FH^{l}_{\mathbf{i}+1/2\mathbf{e}_l} \equiv FL^{l}_{\mathbf{i}+1/2\mathbf{e}_l} + A^{l}_{\mathbf{i}+1/2\mathbf{e}_l}, \tag{8}$$

where (8) defines the residual A-flux, which has a sense of correcting *at least* the first-order truncation error terms in the transport fluxes of the low-order scheme, i.e.,

$$A^{l}_{\mathbf{i}+1/2\mathbf{e}_l} \sim \Delta t \cdot \mathcal{C}(\Delta X, \Delta t) + HOT, \tag{9}$$

where HOT has a usual meaning of the "higher order terms." Because of this compensation of the leading truncation-error term in a low-order scheme the A-flux is traditionally referred to as the "antidiffusive" flux. Using (8) in (7) results in

$$\psi_{\mathbf{i}}^{n+1} = \Psi_{\mathbf{i}}^{n+1} - \sum_{l=1}^{M} \left(A^{l}_{\mathbf{i}+1/2\mathbf{e}_l} - A^{l}_{\mathbf{i}-1/2\mathbf{e}_l}\right), \tag{10}$$

where "Ψ" denotes the solution given by the low-order scheme, which by assumption satisfies

$$\psi_{\mathbf{i}}^{\mathrm{MAX}} \geqslant \Psi_{\mathbf{i}}^{n+1} \geqslant \psi_{\mathbf{i}}^{\mathrm{MIN}}, \tag{11}$$

where ψ_i^{MAX} and ψ_i^{MIN} are yet unspecified maximal and minimal values of the scalar within the ith grid box that achieve the monotonicity of the scheme. Their explicit form will be discussed later in this section. Inasmuch as Ψ_i^{n+1} preserves the monotone character of the transported field, (11), the eventual oscillatory behavior in ψ_i^{n+1} comes from overestimating the magnitude of certain A-fluxes. Thus, to ensure ripple-free solutions it is sufficient to appropriately limit A-fluxes such that

$$\tilde{A}^l_{i+1/2e_l} = C^l_{i+1/2e_l} \cdot A^l_{i+1/2e_l}, \tag{12}$$

where C-coefficients, that in general are functions of the low- and high-order solutions on the grid, are determined from the set of constraints

$$0 \leqslant C^l_{i+1/2e_l} \leqslant 1 \tag{13}$$

and

$$\psi_i^{MAX} \geqslant \tilde{\psi}_i^{n+1} = \Psi_i^{n+1} - \sum_{l=1}^{M} (\tilde{A}^l_{i+1/2e_l} - \tilde{A}^l_{i-1/2e_l}) \geqslant \psi_i^{MIN}. \tag{14}$$

When $C^l_{i+1/2e_l}$ is equal to zero or unity the resulting transport flux in (14) becomes $FL^l_{i+1/2e_l}$ or $FH^l_{i+1/2e_l}$, respectively. The assumed convergence of the low-order schemes involved in (8) together with (9), (12), and (13) ensure the convergence of the $\tilde{\psi}$-solutions in (14) as $\Delta X, \Delta t \to 0$.

The constraints in (13) and (14) allow one to derive formally (see Appendix) the explicit form of the C-coefficients, and consequently, the explicit form of the limited antidiffusive fluxes in (12). The derivation provides maximized $\tilde{A}$-fluxes in (12) satisfying constraints (13) and (14):

$$\tilde{A}^l_{i+1/2e_l} = \min(1, \beta_i^{\downarrow}, \beta^{\uparrow}_{i+e_l})[A^l_{i+1/2e_l}]^+ + \min(1, \beta_i^{\uparrow}, \beta^{\downarrow}_{i+e_l})[A^l_{i+1/2e_l}]^-. \tag{15}$$

where

$$\beta_i^{\uparrow} \equiv \frac{\psi_i^{MAX} - \Psi_i^{n+1}}{A_i^{IN} + \varepsilon}; \qquad \beta_i^{\downarrow} \equiv \frac{\Psi_i^{n+1} - \psi_i^{MIN}}{A_i^{OUT} + \varepsilon} \tag{16a), (16b)}$$

and A_i^{IN}, A_i^{OUT} are the absolute values of the total incoming and outgoing A-fluxes, (8), from the ith grid box, respectively. ε is a small value, e.g., $\sim 10^{-15}$, which has been introduced herein, to allow for efficient coding of β-ratios when A_i^{IN} or A_i^{OUT} vanish. Equations (14), (15), (8), (16a), and (16b) constitute a general, arbitrary dimensional form of the FCT algorithm discussed by Zalesak [7] (the formulas (14), (14′) in [7] are not required to preserve monotonicity and, in our experience, they are responsible for certain pathological behaviors of the FCT schemes, cf., [8]). The arbitrary dimensionality of the procedure in [7] contrasts with the alternate-direction approach utilized by most other monotone schemes.

In order to determine $\beta_{\mathbf{i}}^{\uparrow}$ and $\beta_{\mathbf{i}}^{\downarrow}$ uniquely one must specify the limiter $\psi_{\mathbf{i}}^{\mathrm{MAX}}$, $\psi_{\mathbf{i}}^{\mathrm{MIN}}$ in (16a), (16b). The simple, standard limiter [7] is

$$\psi_{\mathbf{i}}^{\mathrm{MAX}} = \max_{l}(\psi_{\mathbf{i}-\mathbf{e}_l}^{n}, \psi_{\mathbf{i}}^{n}, \psi_{\mathbf{i}+\mathbf{e}_l}^{n}, \Psi_{\mathbf{i}-\mathbf{e}_l}^{n+1}, \Psi_{\mathbf{i}}^{n+1}, \Psi_{\mathbf{i}-\mathbf{e}_l}^{n+1}) \tag{17a}$$

$$\psi_{\mathbf{i}}^{\mathrm{MIN}} = \min_{l}(\psi_{\mathbf{i}-\mathbf{e}_l}^{n}, \psi_{\mathbf{i}}^{n}, \psi_{\mathbf{i}+\mathbf{e}_l}^{n}, \Psi_{\mathbf{i}-\mathbf{e}_l}^{n+1}, \Psi_{\mathbf{i}}^{n+1}, \Psi_{\mathbf{i}-\mathbf{e}_l}^{n+1}). \tag{17b}$$

The low-order, nonoscillatory Ψ-solutions appearing in (17a), (17b) constitute the original Boris and Book [4] limiter. This limiter effectively prevents development of spurious oscillations in an arbitrary flow field. Zalesak [7] extended the original limiter onto the local extrema of the solution at the previous time step. The goal of this extension is to improve the predictions in incompressible flows where the only extrema allowed in an arbitrary grid point are those that were present in its immediate environment (determined by the CFL stability criteria) at the previous time step.

3.2. *FCT Option of MPDATA*

The formulation of the nonoscillatory option of MPDATA is a straightforward consequence of the discussion presented in the previous section. Note that the transport fluxes for $k \geqslant 2$ in (2) have the sense of A-fluxes in (10). Because all of the transport fluxes in MPDATA always have the form of the donor-cell fluxes (3) and MPDATA is strictly sign preserving, Eq. (15) reduces to the formula for the monotonicity-preserving pseudo velocity

$$[\overset{(\sim)^k}{u_l}_{\mathbf{i}+1/2\mathbf{e}_l}]^{\mathrm{MON}} = \min(1, \beta_{\mathbf{i}}^{\downarrow}, \beta_{\mathbf{i}+\mathbf{e}_l}^{\uparrow})[\overset{(\sim)^k}{u_l}_{\mathbf{i}+1/2\mathbf{e}_l}]^{+} + \min(1, \beta_{\mathbf{i}}^{\uparrow}, \beta_{\mathbf{i}+\mathbf{e}_l}^{\downarrow})[\overset{(\sim)^k}{u_l}_{\mathbf{i}+1/2\mathbf{e}_l}]^{-}, \tag{18}$$

where $k = 2, 3, \ldots, IORD$ and the transport of nonnegative scalars has been assumed. In the case of the advection of nonpositive scalars $\uparrow$ replaces $\downarrow$ and vice versa. The $\beta_{\mathbf{i}}^{\uparrow}$ and $\beta_{\mathbf{i}}^{\downarrow}$ ratios take an explicit form

$$\beta_{\mathbf{i}}^{\uparrow} = \frac{\psi_{\mathbf{i}}^{\mathrm{MAX}} - \psi_{\mathbf{i}}^{(*)^{k-1}}}{\sum_{l=1}^{M} \frac{\Delta t}{\Delta X^l}([\overset{(\sim)^k}{u_l}_{\mathbf{i}-1/2\mathbf{e}_l}]^{+}\psi_{\mathbf{i}-\mathbf{e}_l}^{(*)^{k-1}} - [\overset{(\sim)^k}{u_l}_{\mathbf{i}+1/2\mathbf{e}_l}]^{-}\psi_{\mathbf{i}+\mathbf{e}_l}^{(*)^{k-1}}) + \varepsilon} \tag{19a}$$

$$\beta_{\mathbf{i}}^{\downarrow} = \frac{\psi_{\mathbf{i}}^{(*)^{k-1}} - \psi_{\mathbf{i}}^{\mathrm{MIN}}}{\sum_{l=1}^{M} \frac{\Delta t}{\Delta X^l}([\overset{(\sim)^k}{u_l}_{\mathbf{i}+1/2\mathbf{e}_l}]^{+}\psi_{\mathbf{i}}^{(*)^{k-1}} - [\overset{(\sim)^k}{u_l}_{\mathbf{i}-1/2\mathbf{e}_l}]^{-}\psi_{\mathbf{i}}^{(*)^{k-1}}) + \varepsilon} \tag{19b}$$

and (17a), (17b) become

$$\psi_{\mathbf{i}}^{\mathrm{MAX}} = \max_{l}(\psi_{\mathbf{i}-\mathbf{e}_l}^{n}, \psi_{\mathbf{i}}^{n}, \psi_{\mathbf{i}+\mathbf{e}_l}^{n}, \psi_{\mathbf{i}-\mathbf{e}_l}^{(*)^{k-1}}, \psi_{\mathbf{i}}^{(*)^{k-1}}, \psi_{\mathbf{i}-\mathbf{e}_l}^{(*)^{k-1}}) \tag{20a}$$

$$\psi_{\mathbf{i}}^{\mathrm{MIN}} = \min_{l}(\psi_{\mathbf{i}-\mathbf{e}_l}^{n}, \psi_{\mathbf{i}}^{n}, \psi_{\mathbf{i}+\mathbf{e}_l}^{n}, \psi_{\mathbf{i}-\mathbf{e}_l}^{(*)^{k-1}}, \psi_{\mathbf{i}}^{(*)^{k-1}}, \psi_{\mathbf{i}-\mathbf{e}_l}^{(*)^{k-1}}) \tag{20b}$$

which completes the nonoscillatory option of MPDATA. As in the original version, the FCT option allows for an arbitrary number of corrective iterations, where the "high-order" solution in (14) becomes the "low-order" solution in the next iteration. We have verified in a series of elementary tests that the effect of the consecutive iterations is similar to that in the basic version of MPDATA, i.e., each iteration increases the accuracy of calculations but the rate of improvement decreases quickly with iterations, leaving $IORD = 4$ a practical maximum (cf., Section 4 in [2] and Section 4 in [3]). Since the developments reported in [2] and [3] modified either the physical or the pseudo velocity field, they are also applicable with (18)–(20).

4. Elementary Tests and Accuracy Considerations

In [3] we demonstrated that MPDATA is a reliable, accurate, and convenient tool for geophysical fluid dynamics applications. Consequently, in the current paper the scheme in Eqs. (2)–(5) will be considered a reference state for the nonoscillatory option described in the previous section. The nonoscillatory option, by design, prevents development of the dispersive ripples. Thus, our major concern is not how well the scheme preserves the monotone character of the transported field but rather how it affects the accuracy of the solutions obtained with the original version of the algorithm. The intension of this section is to document accuracy characteristics of the nonoscillatory MPDATA and to indicate certain specific advantages of the scheme that are important for practical applications.

A number of important aspects on the accuracy of advection algorithms may be assessed through analysis of the surfaces of the truncation error $\mathcal{O}(\Delta t^p, \Delta X^q)$ as $\Delta X, \Delta t \to 0$ in a one-dimensional constant coefficient case. In contrast to linear advection schemes, formal evaluation of the truncation error for the nonlinear algorithms can be cumbersome. Instead, one may consider a simple empirical test, which is an extension of the convergence test employed in [2, 3]. For the purpose of the test we assume uniform advection of the one-dimensional Gaussian distribution $\psi(x, t_0) = (1/\sigma\sqrt{2\pi}) \exp(-(x - x_0)^2/2\sigma^2)$. After an arbitrary chosen *fixed* time, $T = NT \cdot \Delta t(\alpha, \Delta X)$ ($\alpha \leqslant 1$ is the Courant number and NT is the variable number of the time steps) the average error per spatial increment and per unit of time between the numerical and analytical solutions is evaluated as

$$TRER(\alpha, \Delta X) = \frac{1}{T}\left[\sum_{i=1}^{NX} (\psi(T, x_i) - \psi_i^{NT})^2/NX\right]^{1/2}, \tag{21}$$

where $\psi(T, x_i)$, ψ_i^{NT} are the analytical and numerical solutions, respectively, at the point (T, x_i). *TRER*, when multiplied by T, has the sense of a cumulative in T and average per grid increment truncation error of an employed scheme. Dividing ΔX successively by 2 and evaluating *TRER* for $0.05 \leqslant \alpha \leqslant 0.95$ with the Courant number increment $\Delta\alpha = 0.05$ results in surfaces defined by (21).

Figure 1 displays isolines of $\log_2$ *TRER* for the $IORD = 2$ version of MPDATA

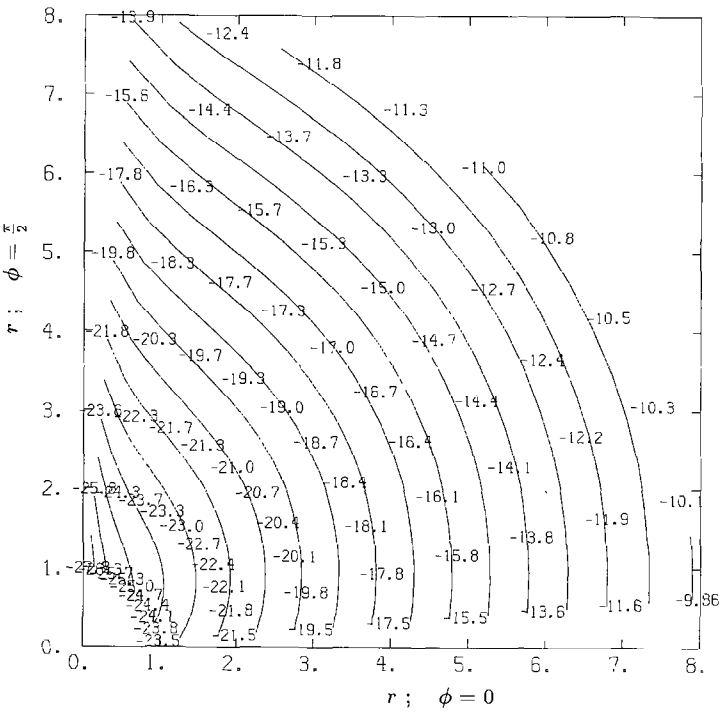

FIG. 1. Isolines of $\log_2(TRER)$ for the $IORD=2$ version of MPDATA, in the polar system of coordinates. The radius has the sense of the grid increment where numbers on axes indicate powers of 2 in the coefficient multiplying the finest resolution; the polar angle represents the Courant number varying from 0 to 1 for angles between 0 and $\pi/2$, respectively. The numerical values of the field are displayed for every second point in the angular (Courant number) direction.

in the polar system of coordinates, where the radius $r=\log_2(\Delta X/\Delta X_8)+8$ (ΔX_8 is the largest grid increment employed in the test) and the polar angle $\phi=\alpha(\pi/2)$. For $r=8$ the dispersion of the initial distribution, σ, is covered by 1.5 grid intervals and for $r=1$ it is covered by 192 grid increments. The time of integration, T, has been chosen such that the solution advects over the one grid increment for $r=8$ and 128 increments for $r=1$. The numbers displayed along the arcs of constant radius are the values of $\log_2 TRER$. Comparing these values along the rays of constant Courant number (constant ϕ) shows that $\log_2 TRER$ decreases in -2 increments with doubling the resolution as ΔX, $\Delta t \to 0$. This demonstrates the second-order convergence rate of the $IORD=2$ version of MPDATA in accord with our previous analysis in [2, 3]. Figure 2 shows $\log_2(TRER)$ for the $IORD=3$ version of MPDATA. The second corrective iteration in the scheme shifts the entire surface down increasing the overall accuracy and it deforms the surface along the $\alpha=0.5$ line, resulting in the depression of the third-order convergence rate. Additional corrective iterations increase accuracy only slightly. Figure 3 shows the error-surface for the $IORD=2$ nonoscillatory version of MPDATA. A comparison of

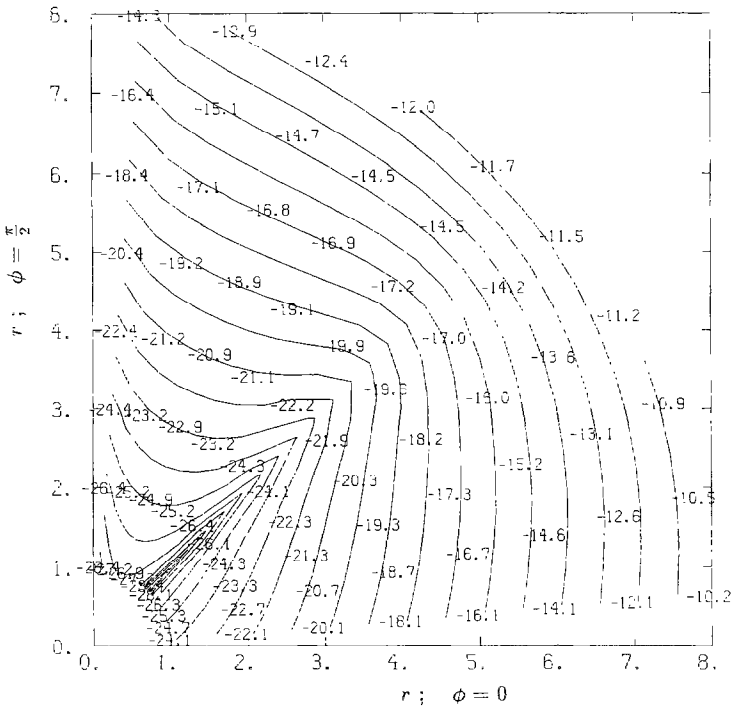

FIG. 2. Isolines of $\log_2(TRER)$ for the $IORD = 3$ version of MPDATA.

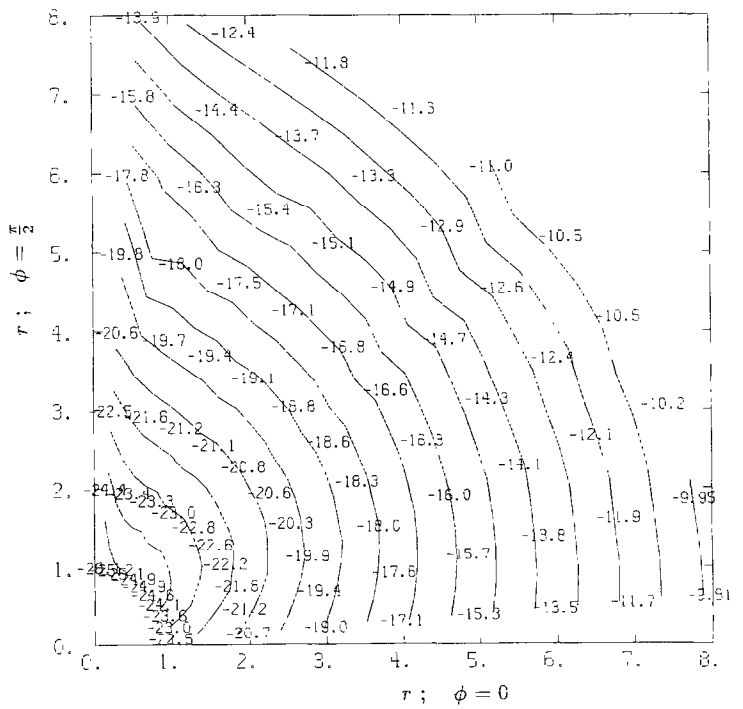

FIG. 3. Isolines of $\log_2(TRER)$ for the $IORD = 2$ nonoscillatory version of MPDATA.

Figs. 3 and 1 shows that at low resolutions, FCT modification has little effect on the accuracy of the algorithm. However, as ΔX, $\Delta t \to 0$ there is a slight degradation in the convergence rate from 2 to ~ 1.8. Similar results were obtained for the $IORD = 3$ version of MPDATA.

The accuracy characteristics of an arbitrary FCT algorithm depend on the choice of the low- and high-order schemes employed in the procedure (Section 3). Figure 4 shows the result of the convergence test for the common donor-cell/leapfrog FCT scheme [7]. A comparison of Figs. 3 and 4 indicates, that in general the non-oscillatory MPDATA converges faster and is more accurate than the donor-cell/leapfrog FCT scheme. For small Courant numbers the latter scheme has a ~ 1.7 convergence rate, slightly slower than the nonoscillatory MPDATA. For large Courant numbers, however, its convergence rate degrades considerably decreasing to values smaller than unity. The reason for this slow convergence rate is the inconsistent anisotropy of the truncation error distribution of the two schemes mixed by the FCT procedure. A comparison of the error surfaces of the donor-cell and the second-order leapfrog schemes showed that the donor-cell scheme, despite its first-order convergence rate, is actually more accurate than the second-order leapfrog scheme for large Courant numbers at the resolutions considered. The latter is related to the faster diminishing phase-error in the donor-cell than in the leapfrog

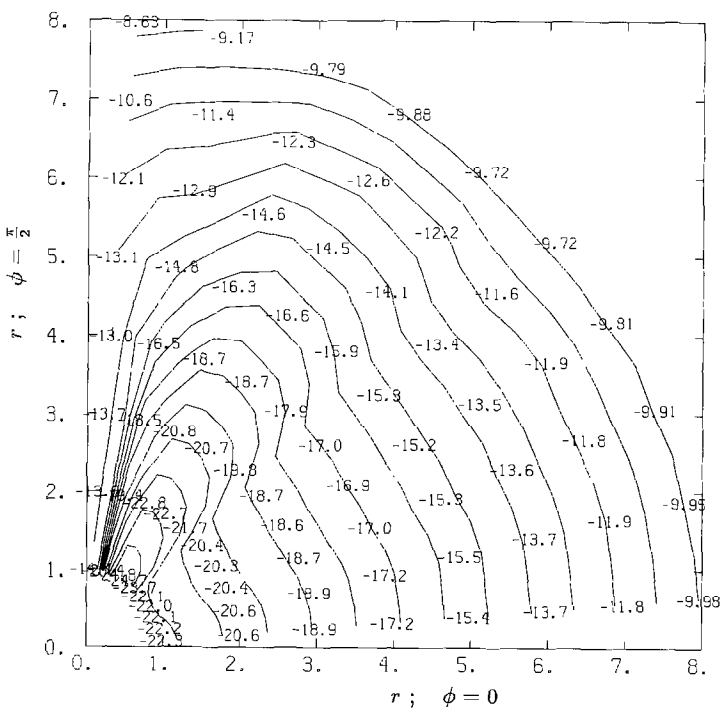

FIG. 4. Isolines of $\log_2(TRER)$ for the donor-cell/leapfrog FCT scheme.

scheme as $\alpha \to 1$ (cf., Table III in [4]). The nonoscillatory option of MPDATA is free of the above-mentioned problem because the subsequent corrective iterations affect only the amplitude errors and retain the phase-error of the donor-cell scheme (Section 4 in [3]).

The nonoscillatory MPDATA has been compared with other, elementary FCT schemes. As revealed by the convergence tests, the nonoscillatory MPDATA is more accurate than the FCT scheme based on the dissipative second-order Crowley algorithm, and for $\alpha > \sim 0.5$ it is also more accurate than the FCT version of fourth-order accurate in the space leapfrog scheme and the FCT version of the second-order Crowley scheme with the fourth-order approximation to the transport fluxes [9]. The FCT scheme based on the "constant-grid flux" fourth-order dissipative algorithm of Tremback *et al.* [10] has at least twice the accuracy of the nonoscillatory MPDATA. No analyzed FCT algorithms exceed second-order convergence rate as a result of the centered approximation of the flux derivatives in (11). The deviations towards convergence rates of less than 2.0 are attributed to the fact that, in order to ensure monotonicity of the final algorithm, the first-order error terms in the low-order scheme employed in the FCT procedures cannot be totally compensated at every grid point [11].

A more pragmatic illustration of the considerations above is provided by the one-dimensional uniform advection test of the irregular signal

$$\phi(x, t_0) = 2 + \phi_0(x)\left(1 + 0.3 \sin\left(\frac{2\pi}{9\,\Delta X} x\right)\right)\left(1 + 0.4 \sin\left(\frac{2\pi}{10\,\Delta X} x\right)\right), \tag{22}$$

where

$$\phi_0(x) = \begin{cases} -1 & \text{if} \quad 8 \leqslant x \leqslant 28 \\ 1 & \text{if} \quad 28 < x \leqslant 39. \end{cases} \tag{23}$$

with $\alpha = 0.5$ and $\Delta X = 1$. The choice of the signal and the spatial resolution places the results of the test in the $r \geqslant \sim 5$ portion of the $\log_2(TRER)$ surfaces discussed earlier. Figure 5a shows the results of the test after 80 time-steps for the $IORD = 3$ version of MPDATA (dashed line) and the nonoscillatory version of this scheme (thin solid line). The heavy solid line represents the analytic solution. Comparison of the three curves shows that the primary effect of the FCT modification is to remove the overshoot and the undershoot present in the original solution. Figure 5b shows the results of the same test but for the traditional FCT algorithm based on the donor-cell and the leapfrog scheme. Although the FCT procedure efficiently removes the dispersive ripples, the amplitudes of the initial perturbations are severely damped at the cost of the improving phase-error. Similar results were obtained for the FCT version of the second-order Crowley schemes. Neither of the schemes considered is capable of resolving the fine details of the initial condition. The superiority of the MPDATA is questionable when compared with the fourth-order accurate dissipative scheme [10] and its FCT version, Fig. 5c.

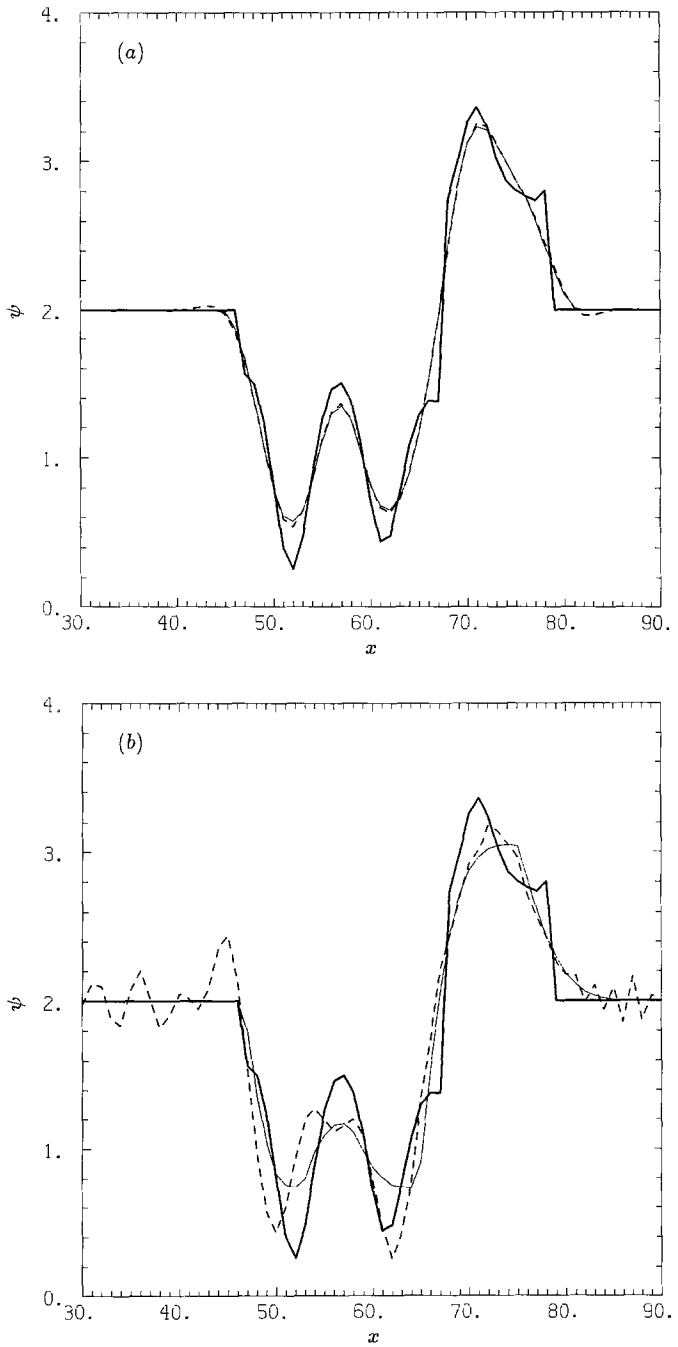

FIG. 5. Uniform advection of the irregular signal (heavy solid lines) with oscillatory schemes (dashed lines) and their nonoscillatory versions (thin solid lines): (a) the $IORD = 3$ MPDATA; (b) the second-order accurate leapfrog scheme; (c) fourth-order accurate dissipative scheme in [10].

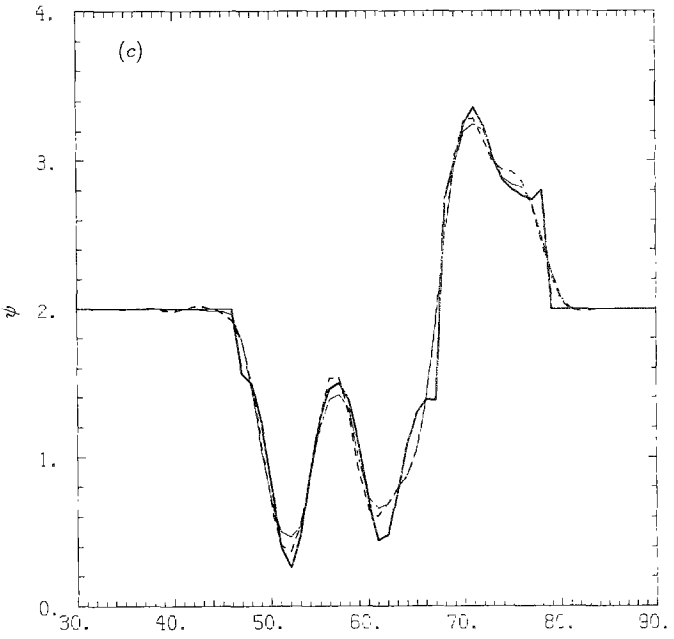

FIGURE 5 (*continued*)

The examples presented illustrate the advantages of the nonoscillatory MPDATA over the more traditional FCT algorithms based on the second-order accurate leapfrog-type or the dissipative advection schemes. The primary reason for the better performance of the MPDATA is the consistent phase-error in the low- and the high-order schemes mixed by the FCT procedure. An apparent advantage of the MPDATA over the leapfrog-type algorithms is the common (for the dissipative schemes) requirement of the one-time level storage of the transported field. The higher order accurate dissipative advection scheme [10] employed in the FCT procedure, although attractive according to the one-dimensional analysis, does not have its multidimensional counterpart, which limits its applications to the alternate-direction (time-splitting) approach. This immediately limits the practicality, especially from our viewpoint, since in the class of geophysical fluid dynamics applications addressed (cf., [3] and Section 5 of this paper), time-splitting is not allowed. Another weak point of these algorithms is that their fast convergence, and the resulting excellent accuracy, is limited to uniform-grid calculations and the particular form of the continuity equation in (1).

For the sake of completeness we show in Fig. 6 the results of the rotating cone test from [2, 3]. This test has been used in [3] to document the nonoscillatory behavior of the MPDATA near "zeros" of the transported field and the lack of invariance of the scheme with respect to the addition of a constant (see Section 2 of this paper). All solutions in Figs. 6a–d are shown after six revolutions of the cone (3768 time steps) whose initial height is equal to the size of the reference spike in

the upper right corner of every plate. Figures 6a–b are after Figs. 8 and 9 in [2] and Fig. 6c is after Fig. 2 in [3] and they represent, respectively, solutions for $IORD = 2$ and $IORD = 3$ MPDATA with a zero background value and $IORD = 2$ MPDATA with a large constant background. As discussed in [3], the addition of the large constant improves the overall accuracy of the scheme but at the cost of dispersive ripples, Fig. 6c. The solution shown in Fig. 6d is equivalent to that in Fig. 6c, except that it has been obtained with the $IORD = 2$ nonoscillatory version of the MPDATA. It is apparent in the figure that the ripples disappeared without noticeable degrading of the overall accuracy of the solution. The latter is consistent

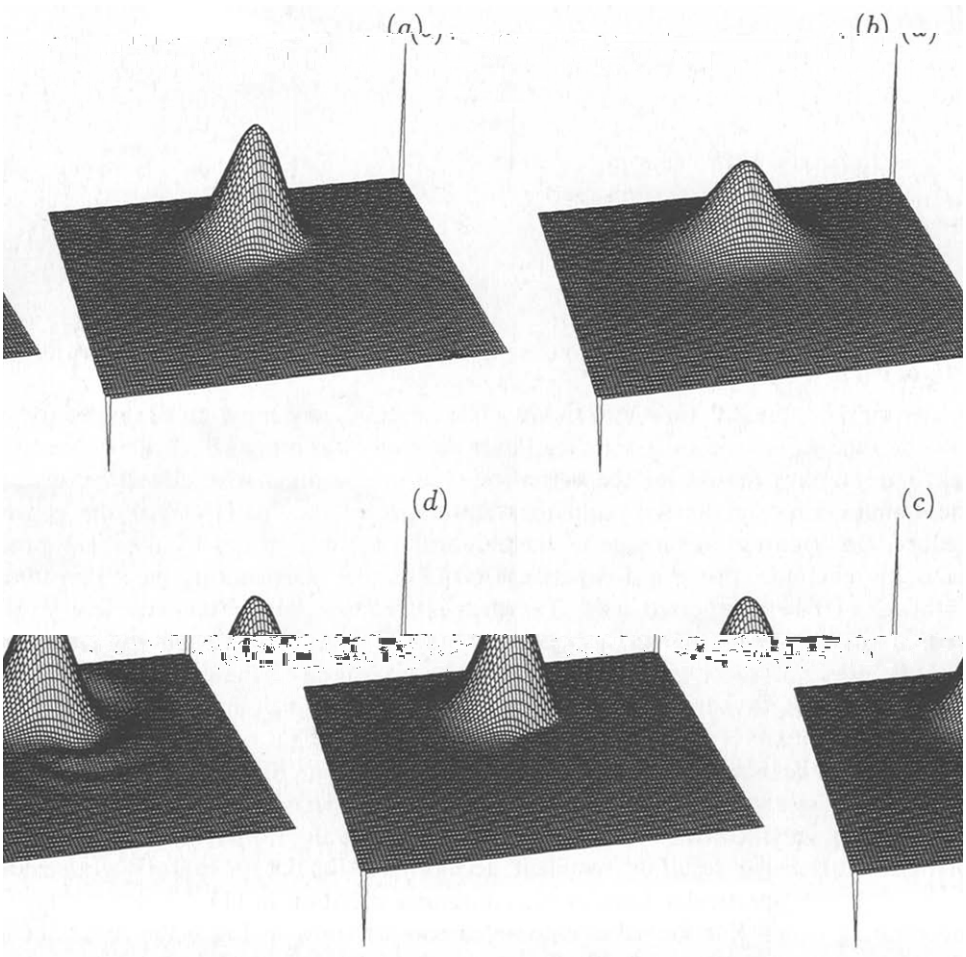

FIG. 6. The rotating cone test from [2, 3]. All solutions are shown after 3768 time steps (six revolutions of the cone). The reference spikes in the upper-right and the lower-left corners represent the initial- and minus half of the initial-height of the cone: (a) $IORD = 2$ MPDATA with zero background value; (b) $IORD = 3$ with zero background value; (c) $IORD = 2$ with large constant background value; (d) $IORD = 2$ nonoscillatory option of MPDATA with the same as in (c) large constant background.

with the results of the convergence test and the irregular-signal advection test discussed earlier in this section. It is worth noting that the solution, equivalent to that shown in Fig. 6, obtained with the donor-cell scheme ($IORD = 1$) almost vanishes [1, Fig. 2], whereas the results obtained for the FCT version of the second-order multidimensional Crowley scheme [8, Fig. 13] are considerably less accurate than these in Fig. 6.

The elementary excercises presented in this section represent only a modest part of a number of different tests performed. In order to verify the performance of the nonoscillatory option of the MPDATA we have repeated most of the tests reported in [2, 3]. In all cases considered the essential outcome was the same as demonstrated herein, i.e., FCT modification to the pseudo velocities in (18) efficiently removed spurious local extrema from the solutions without significantly affecting other properties of the scheme widely documented in previous publications. In all tests performed we have encountered neither the "clipping" nor the "staircases"—pathological behaviors of the FCT schemes often reported in the literature. In the following section we shall demonstrate the satisfactory performance of the scheme in fluid dynamics applications.

5. Examples of Applications

The incorporation of original MPDATA into the anelastic, terrain-following coordinate, dynamic model of Clark [12–14] has been reported in [3]. The model employs the second-order accurate, kinetic energy semi-conserving method of Lilly [15] and Arakawa [16] for integration of the transport equation of momentum, and the second-order accurate MPDATA for all other scalar variables. Because it is the positive definiteness rather than the monotonicity preservation of the transported scalar fields which is essential for most applications of the model, the nonoscillatory modification in (18) has been incorporated into the model as a special-purpose option. The time consumption associated with usage of the nonoscillatory option in the model is approximately equivalent to the time consumption for the default (oscillatory) calculations with $IORD' = 1 + 2(IORD - 1)$ iterations.

Further in this section we discuss examples of applications of the nonoscillatory MPDATA to selected problems of atmospheric fluid dynamics. The two-dimensional algorithm has been applied to the high-resolution experiments of a rising thermal. The three-dimensional algorithm has been applied to the large-eddy simulation of the planetary boundary layer. In the current paper we focus our interests on numerical aspects of the calculations performed—thus we shall discuss physical details of the simulated phenomena only to the extent necessary to emphasize certain aspects of the numerics.

5.1. *Two-Dimensional Thermal Simulation*

Herein, we discuss the rising-thermal experiment similar to that reported in [17], where the authors provided a brief summary of the physical problem and essential

references to adequate numerical and laboratory studies. A dry, slab-symmetric thermal with a diameter of 500 m is placed at 260 m distance above the ground in the center of the horizontal domain. The thermal has a uniform, initial potential temperature excess of 0.5 K relative to the neutral ambient environment. The model domain is 1000 m high and 800 m wide with a uniform grid spacing of 10 m. Free-slip, rigid lid upper and lower boundaries, and periodic lateral boundaries were assumed. The explicit viscosity is zero everywhere. Figure 7a shows the isolines of the potential temperature excess at $t = 10$ min using the $IORD = 2$ nonoscillatory option of MPDATA. The qualitative features of the solution, including sharp gradient zones, formation of the nodes, and the off-axis shift of the buoyancy maxima, agree very well with the simulations reported in [17] that utilize the piecewise parabolic method (PPM) [18]. The authors attributed the above-mentioned features of the solution to the highly inviscid character of calculations offered by the PPM. The conventional techniques considered in [17] were incapable of reproducing sharp gradients, off-axis maxima, and nodal structure of the thermal. Figure 7b shows the solution obtained with the original (oscillatory) version of MPDATA. A comparison of the two figures shows that the overall thermal structure and the essential features of the solution are reproduced by both versions of the scheme. As expected, the oscillatory solution embodies finer scale structures which may be related to the spurious vorticity production due to the local oscillations in the buoyancy field. In contrast to the nonoscillatory solution, the maximum and the minimum of the potential temperature perturbation heavily over- and undershoots relative to the initial values.

5.2. *Large-Eddy Simulation of the Planetary Boundary Layer*

In the following example we discuss a simplification of the heated planetary boundary layer (hereinafter, PBL) experiment of Deardorff [19]. The model domain of 4×4 km in the horizontal and 2 km in the vertical is covered with the uniform grid resolution 50 m. Free-slip, rigid lid upper and lower boundaries and periodic lateral boundaries were assumed. The initial profiles of potential temperature and the water vapour mixing ratio are $\Theta(z) = 283$ and $q_v(z) = 3.5$ for $z \leqslant 0.8$, and $\Theta(z) = 7.5(z - 0.8) + 283$ and $q_v(z) = 1$ for $z > 0.8$, respectively, where the units are, respectively, K, g/kg, and km for Θ, q_v, and z. Zero ambient wind has been assumed. The subgrid-scale turbulence is parametrized with the traditional first-order closure (cf., [12–14]). The PBL is forced with the sensible heat flux of 200 Wm^{-2} with the random noise imposed of maximal amplitude $\pm 5\%$ of the constant component.

Figure 8 shows the resolved Reynolds fluxes of moisture, evaluated after 2 h of simulation with the nonoscillatory (heavy solid line) and the default, oscillatory (thin solid line) version of MPDATA. The dashed line represents the subgrid-scale parametrized fluxes which were in both cases at least two orders of magnitude smaller than the resolved Reynolds fluxes. The presence (absence) of the layer of negative moisture flux above the top of PBL in the calculations with the default (nonoscillatory) MPDATA is apparent in the figure. This negative flux, and the

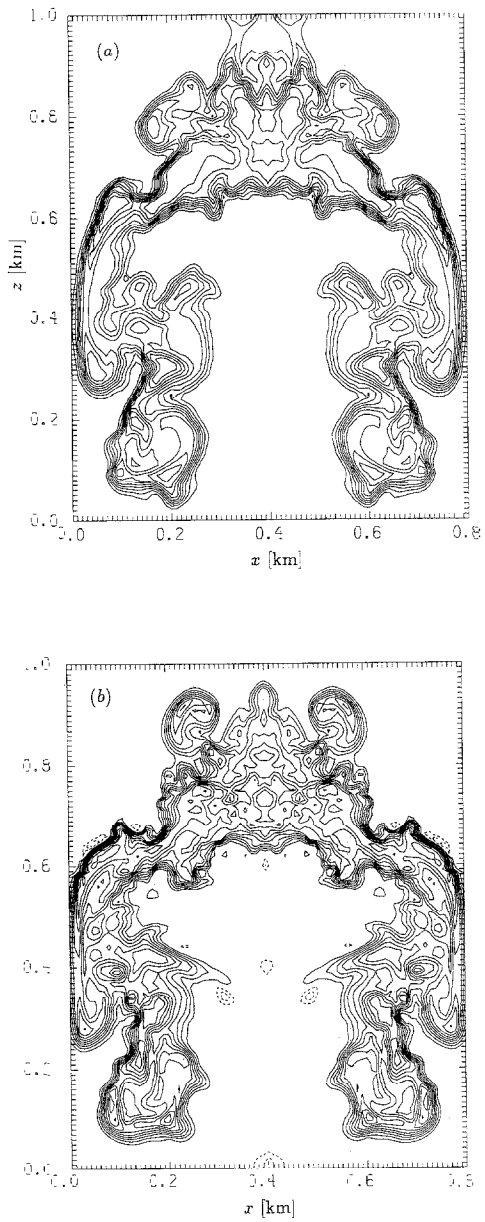

FIG. 7. Plots of the potential temperature perturbation at $t = 10$ min for a rising-thermal experiment. Solid contours represent positive values whereas the dashed contours represent negative. No zero contours are shown although all contour levels are integral increments from the zero line with the interval of 0.5 K: (a) Experiment with $IORD = 2$ nonoscillatory option of MPDATA: (b) experiment with $IORD = 2$ default version of MPDATA. The extrema of the fields are (4.999 K, 0.000 K and (6.401 K, −0.247 K) for (a) and (b), respectively.

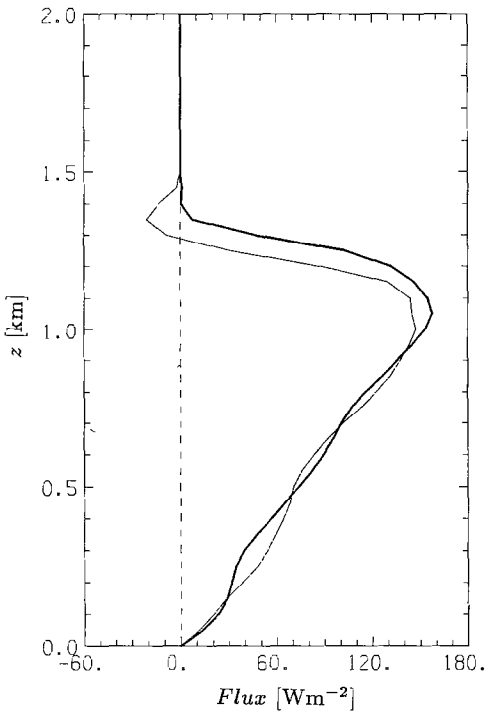

FIG. 8. Profiles of the resolved Reynolds fluxes of moisture for a heated boundary layer experiment. Heavy solid line represents the results for $IORD = 2$ nonoscillatory option of MPDATA whereas the thin solid line represents the results for the default MPDATA, and the dashed line shows the subgrid-scale parametrized flux.

similar structures in the resolved Reynolds fluxes of other thermodynamical variables are a traditional complaint about the large-eddy simulations of turbulent layers. Their relevance to natural PBL was discussed by Deardorff [19], and more recently by Moeng [20], who attributed these features to the spurious effects due to truncation errors at sharp inversions. Since such unrealistic structures may affect eventual parametrization of PBL (one goal of PBL studies) they are usually filtered. Incorporation of the monotone version of MPDATA effectively cures these problems.

6. CONCLUSIONS

1. The nonoscillatory option of the multidimensional positive definite advection transport algorithm (MPDATA) was presented. The monotone version of the scheme merges the flux corrected transport (FCT) methodology with the iterative formalism of the MPDATA. Due to the original design of the MPDATA the non-oscillatory option reduces to a simple mofidication of the pseudo velocity field,

Eq. (18). Because of the specific phase-error properties of the MPDATA, the monotone option effectively prevents development of the dispersive ripples without significantly affecting other properties of the solutions. This has been illustrated by means of elementary tests and examples of applications to atmospheric fluid dynamics problems.

2. An empirical analysis was presented which showed that the nonoscillatory MPDATA appears to be an accurate and competitive tool for applications. A practical advantage of the scheme is a separability of the sign and the monotonicity preservation. This has important economical consequences for these applications which do not necessarily require strict preservation of the monotonicity but do require strict preservations of the sign.

3. The nonoscillatory option, since it only appropriately limits the pseudo velocities in MPDATA, is applicable with all possible developments discussed in the previous publications.

APPENDIX: FCT's Limiting Coefficients

In order to determine the limiting C-coefficients in (12) we note that the grid-box divergence of the transport fluxes may be cast into a sum of total incoming and outgoing fluxes from the grid-box, i.e.,

$$-\sum_{l=1}^{M} (\tilde{A}^l_{\mathbf{i}+1/2\mathbf{e}_l} - \tilde{A}^l_{\mathbf{i}-1/2\mathbf{e}_l}) = \tilde{A}^{\mathrm{IN}}_{\mathbf{i}} - \tilde{A}^{\mathrm{OUT}}_{\mathbf{i}}, \tag{A1}$$

where

$$\tilde{A}^{\mathrm{IN}}_{\mathbf{i}} \equiv \sum_{l=1}^{M} (C^l_{\mathbf{i}-1/2\mathbf{e}_l}[A^l_{\mathbf{i}-1/2\mathbf{e}_l}]^+ - C^l_{\mathbf{i}+1/2\mathbf{e}_l}[A^l_{\mathbf{i}+1/2\mathbf{e}_l}]^-) \tag{A2a}$$

$$\tilde{A}^{\mathrm{OUT}}_{\mathbf{i}} \equiv \sum_{l=1}^{M} (C^l_{\mathbf{i}+1/2\mathbf{e}_l}[A^l_{\mathbf{i}+1/2\mathbf{e}_l}]^+ - C^l_{\mathbf{i}-1/2\mathbf{e}_l}[A^l_{\mathbf{i}-1/2\mathbf{e}_l}]^-). \tag{A2b}$$

Using (A1) in (14) results in

$$\psi^{\mathrm{MAX}}_{\mathbf{i}} \geqslant \tilde{\psi}^{n+1}_{\mathbf{i}} = \Psi^{n+1}_{\mathbf{i}} + \tilde{A}^{\mathrm{IN}}_{\mathbf{i}} - \tilde{A}^{\mathrm{OUT}}_{\mathbf{i}} \geqslant \psi^{\mathrm{MIN}}_{\mathbf{i}}. \tag{A3}$$

Since in (A3) only the inflowing flux increases the value of $\tilde{\psi}^{n+1}_{\mathbf{i}}$ and only the outflowing flux decreases it, then in order to satisfy constraints in (14), it is sufficient to ensure that

$$\psi^{\mathrm{MAX}}_{\mathbf{i}} - \Psi^{n+1}_{\mathbf{i}} \geqslant \max_l(C^l_{\mathbf{i}-1/2\mathbf{e}_l}, C^l_{\mathbf{i}+1/2\mathbf{e}_l})\, A^{\mathrm{IN}}_{\mathbf{i}} \tag{A4a}$$

$$\Psi^{n+1}_{\mathbf{i}} - \psi^{\mathrm{MIN}}_{\mathbf{i}} \geqslant \max_l(C^l_{\mathbf{i}-1/2\mathbf{e}_l}, C^l_{\mathbf{i}+1/2\mathbf{e}_l})\, A^{\mathrm{OUT}}_{\mathbf{i}}. \tag{A4b}$$

where

$$A_{\mathbf{i}}^{\mathrm{IN}} \equiv \sum_{I=1}^{M} \left([A_{\mathbf{i}-1/2\mathbf{e}_I}^I]^+ - [A_{\mathbf{i}+1/2\mathbf{e}_I}^I]^- \right); \tag{A5a}$$

$$A_{\mathbf{i}}^{\mathrm{OUT}} \equiv \sum_{I=1}^{M} \left([A_{\mathbf{i}+1/2\mathbf{e}_I}^I]^+ - [A_{\mathbf{i}-1/2\mathbf{e}_I}^I]^- \right). \tag{A5b}$$

The inequalities (A4a), (A4b) imply that

$$\forall_I \max(C_{\mathbf{i}-1/2\mathbf{e}_I}^I, C_{\mathbf{i}+1/2\mathbf{e}_I}^I) \leqslant \beta_{\mathbf{i}}^{\uparrow}; \qquad \forall_I \max(C_{\mathbf{i}-1/2\mathbf{e}_I}^I, C_{\mathbf{i}+1/2\mathbf{e}_I}^I) \leqslant \beta_{\mathbf{i}}^{\downarrow}, \tag{A6a), (A6b}$$

where

$$\beta_{\mathbf{i}}^{\uparrow} \equiv \frac{\psi_{\mathbf{i}}^{\mathrm{MAX}} - \Psi_{\mathbf{i}}^{n+1}}{A_{\mathbf{i}}^{\mathrm{IN}} + \varepsilon}; \qquad \beta_{\mathbf{i}}^{\downarrow} \equiv \frac{\Psi_{\mathbf{i}}^{n+1} - \psi_{\mathbf{i}}^{\mathrm{MIN}}}{A_{\mathbf{i}}^{\mathrm{OUT}} + \varepsilon}, \tag{A7a), (A7b}$$

and ε is a small value (e.g., 10^{-15}) introduced for coding efficiency of β-ratios when $A_{\mathbf{i}}^{\mathrm{IN}}$ or $A_{\mathbf{i}}^{\mathrm{OUT}}$ vanish. Solving (A6a), (A6b) for C-coefficients results, for every I, in

$$C_{\mathbf{i}+1/2\mathbf{e}_I}^I \leqslant \min(\beta_{\mathbf{i}}^{\uparrow}, \beta_{\mathbf{i}}^{\downarrow}); \qquad C_{\mathbf{i}-1/2\mathbf{e}_I}^I \leqslant \min(\beta_{\mathbf{i}}^{\uparrow}, \beta_{\mathbf{i}}^{\downarrow}) \tag{A8a), (A8b}$$

but since $C_{\mathbf{i}+1/2\mathbf{e}_I}^I \equiv C_{\mathbf{i}+\mathbf{e}_I-1/2\mathbf{e}_I}^I$ and $C_{\mathbf{i}-1/2\mathbf{e}_I}^I \equiv C_{\mathbf{i}-\mathbf{e}_I+1/2\mathbf{e}_I}^I$, the coefficients $C_{\mathbf{i}+1/2\mathbf{e}_I}^I$ and $C_{\mathbf{i}-1/2\mathbf{e}_I}^I$ must also satisfy the inequalities

$$C_{\mathbf{i}+1/2\mathbf{e}_I}^I \leqslant \min(\beta_{\mathbf{i}+\mathbf{e}_I}^{\uparrow}, \beta_{\mathbf{i}+\mathbf{e}_I}^{\downarrow}); \qquad C_{\mathbf{i}-1/2\mathbf{e}_I}^I \leqslant \min(\beta_{\mathbf{i}-\mathbf{e}_I}^{\uparrow}, \beta_{\mathbf{i}-\mathbf{e}_I}^{\downarrow}). \tag{A9a), (A9b}$$

The inequalities (A8), (A9), and (13) reduce to the simple form

$$\forall_{\mathbf{i},I} C_{\mathbf{i}+1/2\mathbf{e}_I}^I \leqslant \min(1, \beta_{\mathbf{i}}^{\uparrow}, \beta_{\mathbf{i}}^{\downarrow}, \beta_{\mathbf{i}+\mathbf{e}_I}^{\uparrow}, \beta_{\mathbf{i}+\mathbf{e}_I}^{\downarrow}). \tag{A10}$$

The inequality (A10) is the sufficient condition for monotonicity of the modified scheme (14). The ratios $\beta_{\mathbf{i}}^{\uparrow}$ and $\beta_{\mathbf{i}}^{\downarrow}$ control overshoots and undershoots, respectively, of the solution at $\mathbf{x}_{\mathbf{i}}$ grid point. Since $A_{\mathbf{i}+1/2\mathbf{e}_I}^I$ in (12) is exclusively, either positive or negative (vanishing $A_{\mathbf{i}+1/2\mathbf{e}_I}^I$ is a trivial case), it exclusively contributes either to the undershoot at $\mathbf{x}_{\mathbf{i}}$ and the overshoot at $\mathbf{x}_{\mathbf{i}+\mathbf{e}_I}$ or the overshoot at $\mathbf{x}_{\mathbf{i}}$ and the undershoot at $\mathbf{x}_{\mathbf{i}+\mathbf{e}_I}$, respectively. Thus, (A10) may be further reduced to

$$C_{\mathbf{i}+1/2\mathbf{e}_I}^I = \min(1, \beta_{\mathbf{i}}^{\downarrow}, \beta_{\mathbf{i}+\mathbf{e}_I}^{\uparrow}) \qquad \text{if} \quad A_{\mathbf{i}+1/2\mathbf{e}_I}^I \geqslant 0, \tag{A11a}$$

$$C_{\mathbf{i}+1/2\mathbf{e}_I}^I = \min(1, \beta_{\mathbf{i}}^{\uparrow}, \beta_{\mathbf{i}+\mathbf{e}_I}^{\downarrow}) \qquad \text{if} \quad A_{\mathbf{i}+1/2\mathbf{e}_I}^I < 0, \tag{A11b}$$

where the equality sign selected in (A11a), (A11b) ensures maximal values of the C-coefficients allowed by the monotonicity constraints and consequently minimal adjustment of the A-fluxes in (12) and the maximal accuracy of the modified algorithm (14). Incorporating (A11a), (A11b) in (12) gives, finally, (15).

REFERENCES

1. P. K. SMOLARKIEWICZ, *Mon. Weather Rev.* **111**, 479 (1983).
2. P. K. SMOLARKIEWICZ, *J. Comput. Phys.* **54**, 325 (1984).
3. P. K. SMOLARKIEWICZ AND T. L. CLARK, *J. Comput. Phys.* **67**, 396 (1986).
4. J. P. BORIS AND D. L. BOOK, *J. Comput. Phys.* **11**, 38 (1973).
5. D. L. BOOK, J. P. BORIS, AND K. HAIN, *J. Comput. Phys.* **18**, 248 (1975).
6. J. P. BORIS AND D. L. BOOK, *J. Comput. Phys.* **20**, 397 (1976).
7. S. T. ZALESAK, *J. Comput. Phys.* **31**, 335 (1979).
8. P. K. SMOLARKIEWICZ, *Mon. Weather Rev.* **110**, 1968 (1982).
9. W. P. CROWLEY, *Mon. Weather Rev.* **96**, 1 (1968).
10. C. J. TREMBACK, J. POWELL, W. R. COTTON, AND R. A. PIELKE, *Mon. Weather Rev.* **115**, 540 (1987).
11. A. HARTEN, J. M. HYMAN, AND P. D. LAX, *Commun. Pure Appl. Math.* **29**, 297 (1976).
12. T. L. CLARK, *J. Comput. Phys.* **24**, 38 (1977).
13. T. L. CLARK, "Cloud Modeling in Three Spatial Dimensions," in *Hailstorms of the Central High Plains*, edited by C. Knight and P. Squires (Colorado Associated University Press, Boulder, 1982), Vol. 1, p. 282.
14. T. L. CLARK AND R. D. FARLEY, *J. Atmos. Sci.* **41**, 329 (1984).
15. D. K. LILLY, *Mon. Weather Rev.* **93**, 11 (1965).
16. A. ARAKAWA, *J. Comput. Phys.* **1**, 119 (1966).
17. R. L. JR. CARPENTER, K. K. DROEGEMEIER, P. R. WOODWARD, AND C. E. HANE, in *Proceedings, 8th Conf. on Numerical Weather Prediction, Baltimore, 1988*, p. 791.
18. P. COLELLA AND P. R. WOODWARD, *J. Comput. Phys.* **54**, 174 (1986).
19. J. W. DEARDORFF, *Bound. Layer Meteor.* **7**, 81 (1974).
20. C.-H. MOENG, *J. Atmos. Sci.* **43**, 2886 (1986).